
Characterization of Shaped Bragg Crystal Assemblies for Narrowband X-Ray Imaging

Introduction

The unique capabilities of a shaped crystal imaging (SCI) system using Bragg crystals are the narrow spectral width ($\lambda/\Delta\lambda > 1000$) (Ref. 1), the up-to-100-fold improvement in throughput over pinhole imaging, and potentially a high spatial resolution ($<2 \mu\text{m}$) (Refs. 2 and 3). Additionally a crystal imaging setup used in backlighting mode is insensitive to spatial nonuniformities in the backlighter intensity distribution because of its limited depth of field.^{4,5} Crystal imaging has been used on both small- to medium-scale facilities^{1,2,6-9} and on larger-scale facilities.^{4,5,10-13} Experimental data from crystal imaging systems have been reported for a variety of spectral lines and crystal materials ranging from ~ 1.5 to 20 keV (Ref. 14).

The major challenges of crystal imaging are the complexity of the alignment and the achievable spatial resolution. Early experiments with SCI systems experienced significant offsets between the surface of the crystal and the diffracting crystal planes. These offsets had to be compensated for by the alignment procedure.⁴ Additionally, even though early experiments showed a very high spatial resolution of $\sim 2 \mu\text{m}$ (Ref. 2), this level of performance could only be repeated in dedicated resolution test setups,³ and most experiments using crystal imaging as a diagnostic reported spatial resolutions of the order of $10 \mu\text{m}$ or worse.^{4,5,9,13,15} Even with the use of aspherically shaped substrates to correct the astigmatism of the off-axis, some illumination at Bragg angles of up to $\sim 6^\circ$ from normal and the higher-order optical aberrations like coma did not substantially improve the observed spatial resolution.⁵

This article describes the study of the imaging performance of a selection of six different crystals using the same cut and mounted on substrates of the same radius of curvature on the Multi-Terawatt (MTW) Laser System¹⁶ at the University of Rochester's Laboratory for Laser Energetics (LLE). Both the offset between the crystal surface and the diffraction planes and the spatial resolution were measured for six crystals from two vendors. Two of the crystals were mounted on aspherical substrates. Additionally, the extent of the reflecting region on

the crystal was inferred and compared with calculations of the rocking curve and the inferred angular acceptance of the crystal, given the width of the spectral line used and the diffraction properties of the crystal.

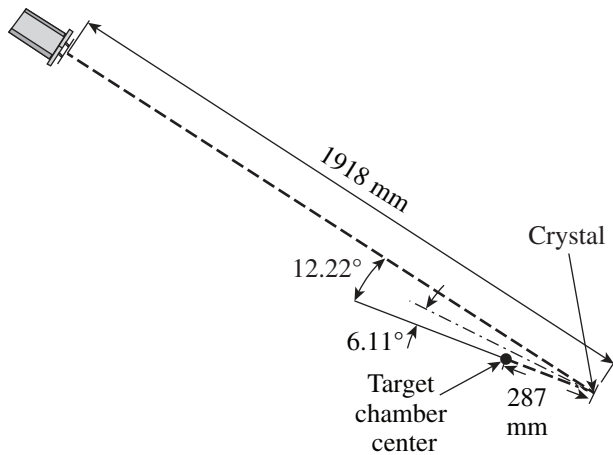
Experimental Setup

The shaped Bragg crystals studied here are designed to reflect the x rays from the Si He $_{\alpha}$ line at ~ 1.865 keV (0.664 nm). The crystals are cut along the 10 $\bar{1}$ 1 plane with a $2d$ spacing of 0.6687 nm. The spherically shaped crystals are 25 mm in diameter with a 0.1-mm thickness. The crystals mounted on the aspheric substrates are the same thickness but are rectangular ($25 \times 10 \text{ mm}^2$), with the longer side perpendicular to the diffraction direction. All substrates had a principal radius of curvature of ~ 500 mm. Since the deviation of the aspheric substrate from a sphere is very small,⁵ at most a few micrometers, the focal shift from the asphericity of the substrate can be neglected compared to the typical manufacturing errors, which are of the order of 0.1% on the principal radius of curvature. Three crystals on spherical substrates, acquired from ECOPULSE,¹⁷ are labeled ECO1-3. The three remaining crystal assemblies were purchased by LLE from a different vendor (INRAD¹⁸) and are labeled LLE3 for the spherical substrate and LLEA1-2 for the aspherical substrates.

For the experiments, the crystal assemblies are set up so that the x rays are incident on the crystal at 83.9° from the surface, the Bragg angle for the Si He $_{\alpha}$ line. This angle corresponds to an angle of incidence of 6.1° (see Fig. 154.60).

The crystals are placed ~ 287 mm from the target (object), and the image is recorded on a Spectral Instruments¹⁹ x-ray CCD (charge-coupled-device) camera placed at a distance of ~ 1918 mm for a magnification of ~ 6.7 .

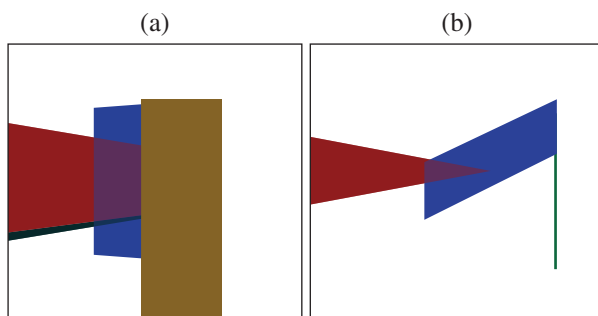
The CCD chip is back-thinned and has 2048×2048 pixels of $13.5 \times 13.5\text{-}\mu\text{m}^2$ size. With a magnification of ~ 6.7 , this translates into a resolution limit of $\sim 2 \mu\text{m}$. The quantum efficiency at ~ 1.865 keV is very high, typically $>80\%$ (Ref. 20) because this energy is directly above the Si K edge.



E27127JR

Figure 154.60
Schematic of the shaped crystal imager setup.

The primary targets, which are illuminated by the laser, are $500\text{-}\mu\text{m}\text{-sq} \times 10\text{-}\mu\text{m}$ -thick silicon wafers. In “backlit mode” [see Fig. 154.61(a)], the laser is defocused to an $\sim 50\text{-}\mu\text{m}$ -diam spot and a “knife-edge” absorbing target, made of a strip of $\sim 12.5\text{-}\mu\text{m}$ -thick aluminum, is placed in the line of sight of the imager covering $\sim 50\%$ of the laser spot size. The absorption of this Al strip is $>99.9\%$ for the Si He_α line.²¹ In “self-emission mode” [see Fig. 154.61(b)], the laser is used at best focus with a spot size of $\sim 5\text{-}\mu\text{m}$ full width at half maximum (FWHM); this spot is directly viewed by the imager. The target is set at an angle of 45° to the incoming laser, and the imager views the target again at 45° to the target normal for a total angle of 90° . In this geometry the effects of the angle of incidence and the view angle cancel, and a round laser spot will appear round on the imager. For some experiments the angle of incidence of the laser was changed to $\sim 3^\circ$, so that the imager



E27253JR

Figure 154.61
Views of the target from the crystal assembly (a) in backlit mode and (b) self-emission mode.

views the target almost edge on to check if the size and shape of the primary x-ray spot affect the x-ray image from the SCI.

For these experiments the MTW laser is operated in two different modes: (1) using a pulse duration of ~ 10 ps at energies of up to 15 J defocused to an $\sim 50\text{-}\mu\text{m}$ FWHM spot size for the backlit setup; (2) with a pulse duration of <1 ps, energies of up to 3 J at best focus ($\sim 5\text{-}\mu\text{m}$ FWHM) for the self-emission setup.

For the experiments with laser-produced plasmas, a $25\text{-}\mu\text{m}$ -thick CH blast shield is mounted on a 30-mm-diam frame placed $\sim 60\text{ }\mu\text{m}$ in front of the crystal to protect it from target debris. For some experiments, additional Al foils are fixed to this frame to reduce the aperture and consequently limit the illuminated area on the crystal. Additionally, a $25\text{-}\mu\text{m}$ -thick black polyimide light shield is mounted in front of the CCD to protect it from scattered light from the high-energy laser pulse.

The crystal imager was aligned using a single-mode optical fiber illuminated by a laser at 635-nm wavelength, which was placed at the center of the target chamber, projecting a cone of light toward the crystal. The CH blast shield and the polyimide light shield were not installed for this alignment procedure.

Images of the optical focus of the tip of the single-mode fibers as recorded by the x-ray CCD are shown in Fig. 154.62 for both (a) a spherical and (b) an aspheric crystal assembly. These images are recorded after optimizing the focal-spot quality for the smallest FWHM. The significant astigmatism with the spherical crystal resulting from the 6.1° angle of incidence is clearly visible in the elongated vertical focus of $\sim 1.8\text{-mm}$ length on the CCD chip. In the horizontal direction, the focus is much narrower and its FWHM corresponds to a width of $\sim 6\text{ }\mu\text{m}$ in the object plane, when the magnification of 6.7 is taken into account. This optical resolution is of the order of the diffraction limit, which is approximately f number $\times \lambda = 7\text{ }\mu\text{m}$, with the f number defined as the object distance (287 mm)/aperture diameter (25 mm). The aspherical crystal shows the expected improvement in the optical focus with the astigmatism almost eliminated and a round central focal-spot shape with an equivalent FWHM in the object plane of $\sim 7\text{ }\mu\text{m}$.

Experimental Data

1. Spatial Resolution

Figure 154.63(a) shows an x-ray image from a spherical crystal (LLE3) in the backlighter configuration. The scale of the image is identical to the image of the optical focus shown in Fig. 154.62. The horizontal width is clearly larger in the

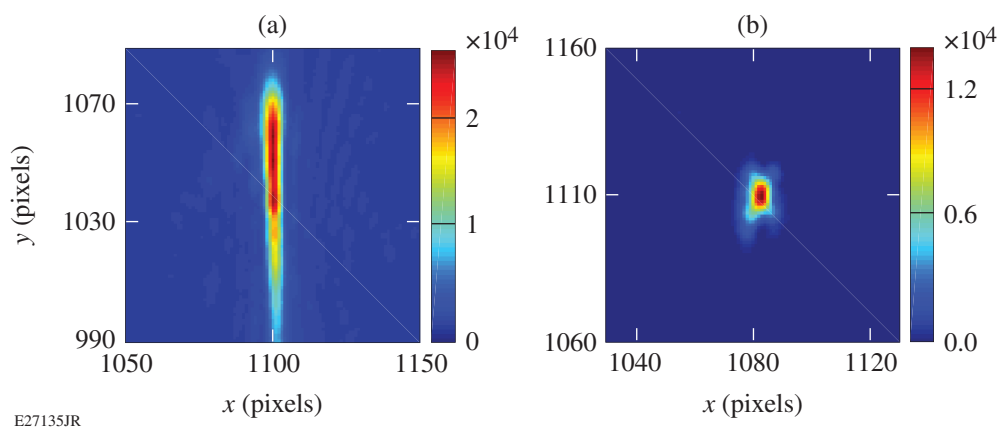


Figure 154.62

Image of the optical focus from the single-mode fiber recorded on the x-ray CCD (charge-coupled device) for (a) a spherical crystal and (b) an astigmatism-corrected asphere.

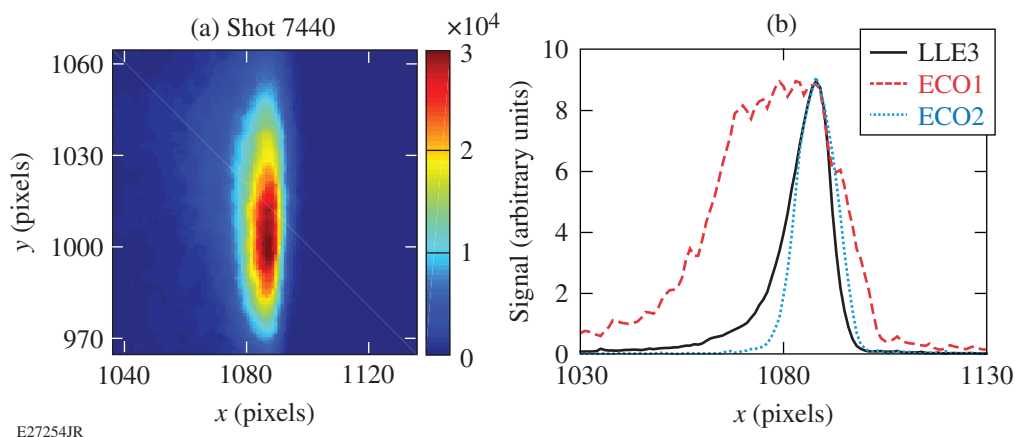


Figure 154.63

(a) X-ray image from a spherical crystal (LLE3) in the backlighting setup. The shadow of the edge is on the right side of the bright feature. (b) Horizontal lineouts through images of three different crystals. [The black solid line is the lineout through the image shown in (a).]

x-ray image compared to the optical focus. The shadow of the absorbing foil [see Fig. 154.61(a)] in front of the emitting laser-heated area is barely visible through the difference in the slope of the falloff on the left and right sides of the peak.

Figure 154.63(b) shows horizontal lineouts through x-ray images for three different crystals, averaged over 11 rows to improve the signal to noise, recorded in backlit mode [the solid black curve corresponds to a lineout of Fig. 154.63(a)]. The shadow of the knife edge can be seen more clearly in the lineouts at the right side. The width of the signal is determined mostly by the alignment tolerances and is not correlated with the resolution. The slope on the right side of the lineout is evaluated for the distance between 90% and 10% of the peak

signal (90–10 distance) as a measure of the spatial resolution of the crystal. Three lineouts are taken for each image, one in the center of the astigmatic feature and one on the top and bottom, respectively. The inferred resolution does not vary significantly across the astigmatic feature, and the changes are of the order of $\sim 1 \mu\text{m}$. The four spherical crystals evaluated by this method show resolutions ranging from ~ 14 to $22 \mu\text{m}$. Up to three images are recorded for each crystal. The analysis of these images shows variations in the measured resolution of the order of $\sim 1 \mu\text{m}$.

X-ray images from a spherical and an aspherical crystal in self-emission mode at a 45° angle of incidence are shown in Figs. 154.64(a) and 154.64(b), respectively. Again the astigma-

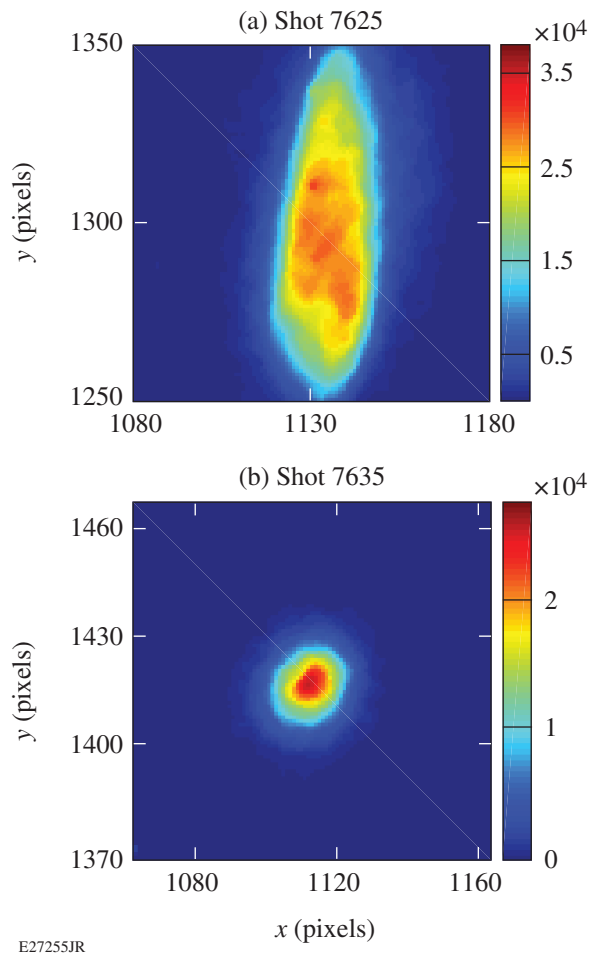


Figure 154.64
X-ray images for a spherical crystal in the self-emission setup for (a) a spherical crystal (ECO1) and (b) an astigmatism-corrected aspherical crystal (LLE-A2).

tism is clearly visible in the image from the spherical crystal and absent from the asphere. Similar to the backlit data, the resolution of the self-emission images was evaluated using the 90–10 distance on a horizontal lineout averaged over 11 rows through the image. Three spherical and two aspherical crystals were evaluated in self-emission mode with measured resolutions ranging from 11 to 44 μm . For the spherical crystals, three lineouts were taken through the astigmatic feature, with the same procedure as used in the backlit mode. Only one crystal (ECO1) showed large differences in resolution of up to $\sim 10 \mu\text{m}$ between the lineouts taken in the center and at the edges of the crystal; all others were within $\sim 1 \mu\text{m}$. Since the image from the aspherical crystals is not elongated, only one lineout was taken for them.

Again, up to three images were recorded for each crystal. The variations of the measured resolution were also of the order of $\sim 1 \mu\text{m}$. Images from 3° angle of incidence shots (not shown

here) show only a slight asymmetry, which indicates that the effects from the finite x-ray spot size are minimal. The evaluated spatial resolutions for the two crystals checked under these conditions are consistent with the 45° data within the errors.

Figure 154.65 summarizes the resolution data of the six evaluated crystals in both backlit and self-emission modes. The errors shown in the figure are the quadrature sum of the variations from the three lineouts and the shot-to-shot variations for the spherical and aspheric crystals. Within errors, the backlighting and self-emission configurations gave consistent results; nevertheless, a large spread of up to a factor of 4 in the measured spatial resolution is observed. For the ECOPULSE crystals, some of the variations in resolution were correlated with the post-polishing etch process, which differed between the three crystal assemblies, so that the effectiveness of the etching could be evaluated. The $2\times$ difference in the resolution for the aspheric assemblies was unexpected because both assemblies were procured at the same time and were presumably prepared the same way. Unfortunately the vendor has not yet disclosed any details of their proprietary manufacturing process.

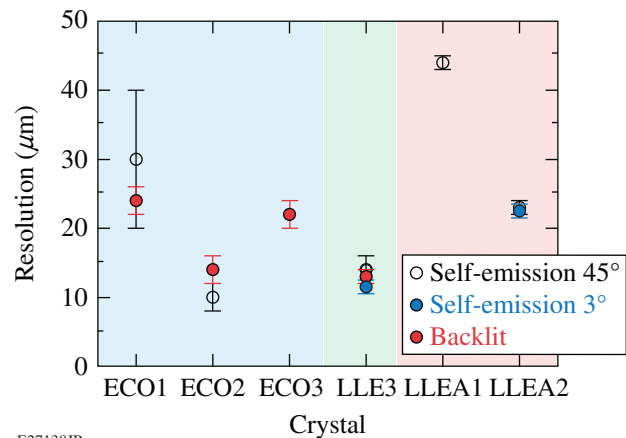
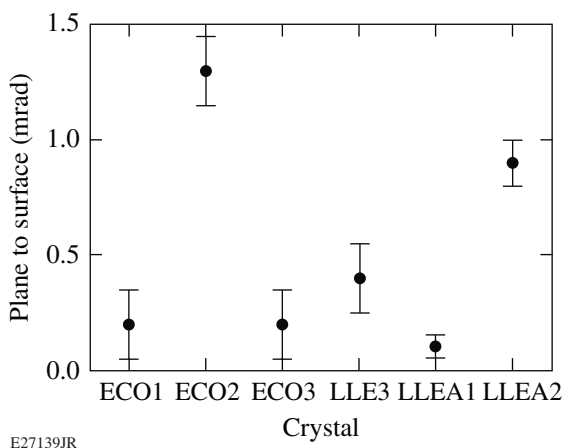


Figure 154.65
Spatial resolution measured for the six individual crystals in both backlit and self-emission geometries.

2. Angle of Surface to the Lattice Plane

Since both the alignment images and the x-ray images are recorded on the same CCD camera and the installation of the CH blast shield and polyimide light shield after the alignment does not significantly affect the alignment of the SCI system, the offset angle ω between the lattice planes and the crystal surface can be determined with high accuracy from the distance d_x between the optical spot and the x-ray spot on the CCD chip (see Fig. 154.66). In a reflecting geometry the offset angle is simply $\omega \sim d_x / (2 * d_i)$, with $d_i \sim 1918 \text{ mm}$ being the distance

from the crystal to the CCD. The errors on the offset angle are caused by the uncertainties in measuring the center of the optical and x-ray spots, respectively. These errors are much smaller for the aspherical crystals than the spherical because of the smaller spot sizes of the aspheres. The measured offsets are all in the diffraction direction (vertical). The horizontal (perpendicular to the diffraction direction) offsets are all well within the error bars, which supports the assumption that the alignment shifts between alignment and x-ray modes are minor and the shifts are dominated by the offset between the lattice planes and the crystal surface. Most of the measured offsets are quite small (<1 mrad); only one crystal shows an untypically large offset angle of ~1.5 mrad. This result indicates that the crystal vendors have largely solved the offset issue. With the typically observed values of <0.5 mrad, the image moves less than 1 mm per 1-m image distance, which is not an issue even on a relatively small CCD chip of 10- to 30-mm size.

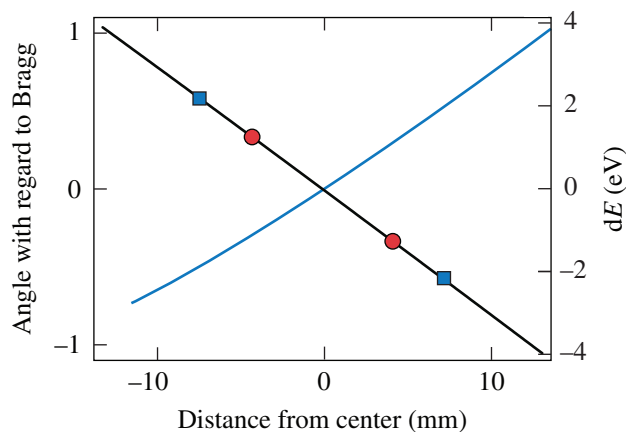


E27139JR

Figure 154.66
Angle of the surface to the lattice plane for the six studied crystals.

3. Illuminated Area on the Crystal

The optical and x-ray images from the spherical crystals can also be used to infer the size of the region on the crystal that actually reflects x rays from the source. A simple 1-D ray trace was set up to calculate the local angle of incidence on the crystal and to correlate the height of the astigmatic feature with the size of the illuminated area on the crystal. This ray trace showed that the 30-mm aperture in front of the crystal, where the blast shield is mounted, limits the vertical aperture to ~16 mm. Figure 154.67 shows the correlation between the distance from the center of the crystal in the vertical direction and the change in angle of incidence from the 6.1° required to fulfill the Bragg condition at the nominal x-ray energy of 1.865 keV of the Si He $_{\alpha}$ line.



E27146JR

Figure 154.67
With the MTW geometry, the Bragg angle changes by $\sim \pm 1^\circ$ over the crystal surface (left axis). The height of the astigmatic focus of 1.8 mm in the optical corresponds to an illuminated height of ~14 mm on the crystal (squares). The 1-mm height of the focus in the x rays corresponds to 8 mm (circles), which translates into a spectral acceptance of ~5 eV, using the Bragg condition, which translates angle into photon energy (right axis).

The ray trace showed that the 1.8-mm measured height of the optical astigmatic feature corresponds to an ~14-mm illuminated height on the crystals, which is in reasonable agreement with the 16-mm vertical limit calculated from the geometry of the setup. The astigmatic features in the x-ray images from the spherical crystals are significantly shorter than the optical features with a length of typically 1 mm, which translates into an illuminated area of ~8 mm on the crystal. With the Bragg condition $\lambda = 2d \sin(\theta)$, the angular variation can be translated into a change in photon energy (right axis of Fig. 154.67). Using the data shown in Fig 154.67, the inferred spectral acceptance for the spherical crystals is ~5 eV. This is considerably larger than the natural line width of the Si He $_{\alpha}$ line, which is well below 1 eV, as calculated from the transition probability.²² The actual width of the spectral line was not measured in these experiments, but data from experiments with Al targets under similar conditions²³ indicate that density, temperature, or flow effects can broaden the spectral lines to widths of the order of 5 to 10 eV.

Summary and Outlook

Six shaped crystal imaging assemblies were evaluated for their imaging quality. None of these assemblies exhibited a similarly large offset angle like the ones reported in early experiments.⁴ The angular offsets were typically below 0.5 mrad, with one crystal assembly at 1.5 mrad. Both values are small enough that these images can be easily used even with small x-ray CCD detectors. The spatial resolution showed a large variation of up to 4 \times between the best and the worst crystals.

So far, one step in the quite-involved manufacturing procedures could be correlated with an improvement in the spatial resolution. For the ECOPULSE crystals, an additional post-polish etch of the crystal surface improves the spatial resolution twofold. This result suggests that subsurface damage from the polishing step might affect the spatial resolution, similar to the effects on the crystal rocking curve reported in the literature.²⁴ According to dynamic diffraction simulations (XOP²⁵ Stepanov x-ray server²⁶), the x-ray extinction length in the crystal is of the order of 2 μm , which makes it plausible that a less-than-perfect crystal structure close to the surface can cause the spatial resolution to degrade. Additionally the height of the reflecting area on the crystal surface could be inferred from the height of the astigmatic focus for the spherical crystals. The $\sim 8\text{-mm}$ measured height corresponds to a range in the Bragg angle of $\sim 12\text{ mrad}$, which is considerably larger than the rocking curve calculated by XOP of $\sim 1\text{ mrad}$. The spectral bandwidth of the reflected x rays of $\sim 5\text{ eV}$ inferred from the range in Bragg angles indicates that the spectral line is significantly broadened from its natural line width. Consequently, this setup cannot be used to measure the rocking curve of the crystals.

In experiments planned for the near future, the spectrum of the x-ray source will be measured with a high-resolution spectrometer so that the linewidth can be directly compared with the inferred values from the imager. Additional experiments will explore changes in magnification and their impact on the spatial resolution.

ACKNOWLEDGMENT

The authors thank E. Baronova from ECOPULSE for the loan of two crystal assemblies.

This material is based upon work supported by the Department of Energy National Nuclear Security Administration under Award Number DE-NA0001944, the University of Rochester, and the New York State Energy Research and Development Authority.

REFERENCES

1. T. A. Pikuz *et al.*, Proc. SPIE **3767**, 67 (1999).
2. Y. Aglitskiy *et al.*, Appl. Opt. **37**, 5253 (1998).
3. E. O. Baronova *et al.*, Instrum. Exp. Tech. **47**, 260 (2004).
4. J. A. Koch *et al.*, Rev. Sci. Instrum. **74**, 2130 (2003).
5. C. Stoeckl, M. Bedzyk, G. Brent, R. Epstein, G. Fiksel, D. Guy, V. N. Goncharov, S. X. Hu, S. Ingraham, D. W. Jacobs-Perkins, R. K. Jungquist, F. J. Marshall, C. Mileham, P. M. Nilson, T. C. Sangster, M. J. Shoup III, and W. Theobald, Rev. Sci. Instrum. **85**, 11E501 (2014).
6. T. Missalla *et al.*, Rev. Sci. Instrum. **70**, 1288 (1999).
7. Ch. Reich *et al.*, Phys. Rev. E **68**, 056408 (2003).
8. S. Le Pape *et al.*, Rev. Sci. Instrum. **79**, 106104 (2008).
9. J. A. King, K. Akli, R. A. Snavely, B. Zhang, M. H. Key, C. D. Chen, M. Chen, S. P. Hatchett, J. A. Koch, A. J. MacKinnon, P. K. Patel, T. Phillips, R. P. J. Town, R. R. Freeman, M. Borghesi, L. Romagnani, M. Zepf, T. Cowan, R. Stephens, K. L. Lancaster, C. D. Murphy, P. Norreys, and C. Stoeckl, Rev. Sci. Instrum. **76**, 076102 (2005).
10. K. Fujita *et al.*, Rev. Sci. Instrum. **72**, 744 (2001).
11. C. Stoeckl, J. A. Delettrez, R. Epstein, G. Fiksel, D. Guy, M. Hohenberger, R. K. Jungquist, C. Mileham, P. M. Nilson, T. C. Sangster, M. J. Shoup III, and W. Theobald, Rev. Sci. Instrum. **83**, 10E501 (2012).
12. C. Stoeckl, G. Fiksel, D. Guy, C. Mileham, P. M. Nilson, T. C. Sangster, M. J. Shoup III, and W. Theobald, Rev. Sci. Instrum. **83**, 033107 (2012).
13. G. Hall *et al.*, Bull. Am. Phys. Soc. **62**, BAPS.2017.DPP.GO7.3 (2018).
14. M. S. Schollmeier and G. P. Loisel, Rev. Sci. Instrum. **87**, 123511 (2016).
15. D. B. Sinar *et al.*, Appl. Opt. **42**, 4059 (2003).
16. V. Bagnoud, in *Frontiers in Optics 2004* (Optical Society of America, Rochester, NY, 2004), Paper FMM2.
17. EcoPulse Inc., Springfield, VA 22152, <http://www.ecopulse.com/> (12 April 2018).
18. Inrad Optics, Northvale, NJ 07647.
19. Spectral Instruments Inc., Tucson, AZ 85745.
20. S. Hubert and V. Prévot, Appl. Opt. **53**, 8078 (2014).
21. CXRO X-Ray Interactions with Matter, http://henke.lbl.gov/optical_constants/ (12 April 2018).
22. NIST Atomic Spectra Database, NIST Standard Reference Database #78, Ver. 5, November 2017, <http://www.nist.gov/pml/data/asd.cfm> (1 June 2016).
23. W. Theobald, C. Stoeckl, P. A. Jaanimagi, P. M. Nilson, M. Storm, D. D. Meyerhofer, T. C. Sangster, D. Hey, A. J. MacKinnon, H.-S. Park, P. K. Patel, R. Shephard, R. A. Snavely, M. H. Key, J. A. King, B. Zhang, R. B. Stephens, K. U. Akli, K. Highbarger, R. L. Daskalova, L. Van Woerkom, R. R. Freeman, J. S. Green, G. Gregori, K. Lancaster, and P. A. Norreys, Rev. Sci. Instrum. **80**, 083501 (2009).
24. E. J. Armstrong, Bell. Syst. Tech. J. **25**, 136 (1946).
25. M. Sánchez del Río and R. J. Dejus, Proc. SPIE **8141**, 814115 (2011).
26. GID_SL on the Web, 19 September 2016, http://x-server.gmca.aps.anl.gov/GID_sl.html (12 April 2018).